HOSTED BY

ELSEVIER

Available online at www.sciencedirect.com

ScienceDirect

Soils and Foundations 60 (2020) 668–682

SOILS AND FOUNDATIONS

www.elsevier.com/locate/sandf

Numerical simulation of a free fall penetrometer deployment using the material point method

Luis Zambrano-Cruzatty *, Alba Yerro

Virginia Tech, United States

Received 8 July 2019; received in revised form 7 April 2020; accepted 18 April 2020
Available online 16 June 2020

Abstract

Free Fall Penetrometer (FFP) testing consist of a torpedo-shaped body freefalling into a soil target. The use of this type of device is becoming popular for the characterization of shallow sediments in near-shore and off-shore environments because it is a fast, versatile, and non-expensive test capable of recording acceleration and pore pressures. In recent years, the data analysis advanced considerably, but the soil behavior during fast penetration is still uncertain. Hence, there is a need to develop numerical models capable of simulating this process to improve its understanding. This paper proposes a numerical framework to simulate the deployment of an FFP device in dry sands using the Material Point Method (MPM). A moving mesh technique is used to ensure the accurate geometry of the FFP device throughout the calculation, and the soil-FFP interaction is modelled with a frictional contact algorithm. Moreover, a rigid body algorithm is proposed to model the FFP device, which enhances the performance of the computation and reduces its computational cost. The sand is simulated by using two constitutive models, a non-associate Mohr-Coulomb (MC) and a Strain-Softening Mohr-Coulomb (SSMC) that reduces, exponentially, the strength parameters with the accumulated plastic deviatoric deformation (Yerro et al., 2016). Variable dilatancy, which reduces as a function of the plastic strain, is also taken into account, and the strain-rate effects have been evaluated in terms of peak friction angle. In general, the behavior predicted by the MPM simulations is consistent with the experimental test. The results indicate that the soil stiffness has a big impact on the deceleration time-history and the development of a failure mechanism, but less influence on the magnitude of the peak deceleration and the penetration depth; the soil dilatancy reduces the FFP rebound, and the FFP-soil contact friction angle and the peak friction angle are highly linked to the peak deceleration.

Keywords: Material point method; Free fall penetrometer; Cone testing; Impact penetration; Sediment characterization; High strain-rate

1. Introduction

Free Fall Penetrometer (FFP) testing is becoming a popular method to characterize shallow sediments because it is fast, cheap, and versatile (Stark et al., 2014). FFP testing usually consists of a torpedo-like device with embedded sensors that free falls through air or water impacting the soil at velocities between 3 and 7 m/s (Stark et al., 2012; Albatal et al., 2017; Albatal, 2018). After the impact, the FFP penetrates the sediment until it stops due to soil reaction forces. Depending on the carried-on sensors, the FFP can record changes in acceleration, pore pressures, among others. The measured changes in acceleration are used to compute the reaction forces acting on the FFP, which include the dynamic effects produced by loading the soil at high strain-rates (HSR). The interpretation of sediment properties still relies on empirical correlations because of the complexities associated with fast impact problems (Stark et al., 2012; Loughlin, 2018; Nazem et al., 2012; Moavenian et al., 2016). Therefore, the development of

Peer review under responsibility of The Japanese Geotechnical Society.
* Corresponding author.
E-mail addresses: luisez@vt.edu (L. Zambrano-Cruzatty), ayerro@vt.edu (A. Yerro).

https://doi.org/10.1016/j.sandf.2020.04.002

reliable numerical models is essential to obtain a more comprehensive understanding of the impact-penetration problem.

The modelling of penetration in geotechnics involving soil-structure impact, such as the FFP testing, installation of dynamic torpedo anchors, or installation of driven piles, is challenging because it has to address device-soil interaction, transient velocities, large soil deformation, hydro-mechanical coupling between soil skeleton and pore fluids (i.e., water and air), and strain-rate strength dependency (Nazem et al., 2012; Moavenian et al., 2016; Sabetamal et al., 2018).

Several techniques have been proposed over the years to simulate FFP deployment or similar problems. The studies using Updated Lagrangian Finite Element Methods (UL FEM) struggle to handle large deformations due to excessive mesh tangling (Smith and Chow, 1982; Mabsout and Tassoulas, 1994; Aubeny and Shi, 2006; Abelev et al., 2009), hence different models are required to simulate a single penetration process. Others (Carter et al., 2010; Nazem et al., 2012; Sabetamal et al., 2013; Liu et al., 2014; Kim et al., 2015; Wang et al., 2015; Sabetamal et al., 2016; Moavenian et al., 2016; Sabetamal et al., 2018), use aggressive re-meshing techniques, such as the Arbitrary Lagrangian Eulerian (ALE) or the Coupled Eulerian Lagrangian (CEL) FEM schemes, to avoid mesh lockup or entanglement. These re-meshing procedures are computationally expensive and can induce errors when tracking state variables of history-dependent materials. On the other hand, there is a clear lack of FFP simulations in non-cohesive soils. This is because the behavior of sands under rapid impact-penetration conditions is difficult to predict. While clays are expected to behave in undrained conditions, sands can have transient drainage behavior (Loughlin, 2018; Albatal, 2018), which complicates the selection of parameters and the assignation of drainage conditions. Moreover, the behavior of sands under HSR is more complicated to characterize than in clays (Mitchell and Soga, 1976). The HSR laboratory testing programs are rare, expensive, and highly complex to perform (Yamamuro et al., 2011; Omidvar et al., 2012), and consequently, only a few constitutive models have been proposed to simulate HSR behavior for sands (Xu and Zhang, 2015).

The objective of this work is to propose a numerical framework capable of simulating FFP penetration in dry sands. First, the Material Point Method (MPM) is proposed as an alternative technique capable of handling large deformation without re-meshing algorithms. Subsequently, the physical characteristics of an FFP penetration laboratory experiment, as well as the geotechnical properties of the sand, are presented. Then, the numerical MPM model is described. In this study, a moving mesh technique, attached to the FFP structure, is considered to ensure a well-defined FFP geometry throughout the calculation. The soil-FFP interaction is modeled by means of a frictional contact algorithm. A rigid body algorithm is proposed to simulate the incompressibility of the FFP and to reduce the computational effort. Finally, the effect of different material properties (i.e., FFP compressibility, contact friction angle, dilatancy, or volumetric change during the penetration, strain-softening effects) are investigated in terms of the kinematic response of the FFP penetration as well as the bearing capacity failure mechanism. The results are compared with the measurements from the physical experiment, and a discussion is established regarding the strain-rate effects.

2. The material point method

The Material Point Method (MPM) was proposed by Sulsky et al. (1995) as an extension of the FLIP Particle in Cell (PIC) method. MPM is a continuum particle-based method that discretizes the material with a set of "material points". Each material point moves attached to the material (i.e. Lagrangian frame) carrying all the updated information (i.e., material state variables, stress, strain, velocity, etc.). MPM also requires a background computational mesh where the governing equations (i.e., momentum balance) are solved. In the original MPM, this mesh is kept fixed throughout the calculation process (i.e., Eulerian frame). Mapping functions are used between the material points and the grid to transfer the required information.

Fig. 1a illustrates the MPM discretization at the beginning of the calculation. The computational MPM cycle consists of three phases: (1) the mapping phase, in which the information carried by the material points is transferred to the surrounding nodes (Fig. 1b); (2) the Lagrangian phase, which consist on solving the governing equations (i.e., linear momentum balance) at the nodes of the grid (Fig. 1c); and (3) the convective phase, in which the updated solution (i.e., acceleration) is mapped back to the material points. At this time, the position of the material points is updated, and the mesh information is discarded (Fig. 1d). The final deformed configuration is shown in Fig. 1e.

Within this particular framework, the limitations associated to Lagrangian (i.e., extreme mesh distortion in large deformation problems) and Eulerian (i.e., difficulties in tracking history-dependent materials) schemes are overcome. These features make the MPM a powerful tool to simulate large deformation problems, including impact and penetration, in history-dependent materials. However, MPM can be affected by numerical artifacts such as cell-crossing instability (Zhou et al., 1999), volumetric locking, and the sporadic occurrence of empty elements in the material domain. These issues, together with the techniques used in this work to reduce their effects, are described in more detail in Yerro et al. (2015). Besides, since Sulsky's pioneer publication (Sulsky et al., 1995), MPM has been extended with the contributions of several authors, in particular, Bardenhagen et al. (2000) and Bardenhagen et al. (2001), who first introduced a contact algorithm for the simulation of friction interaction between different bodies, or Zabala

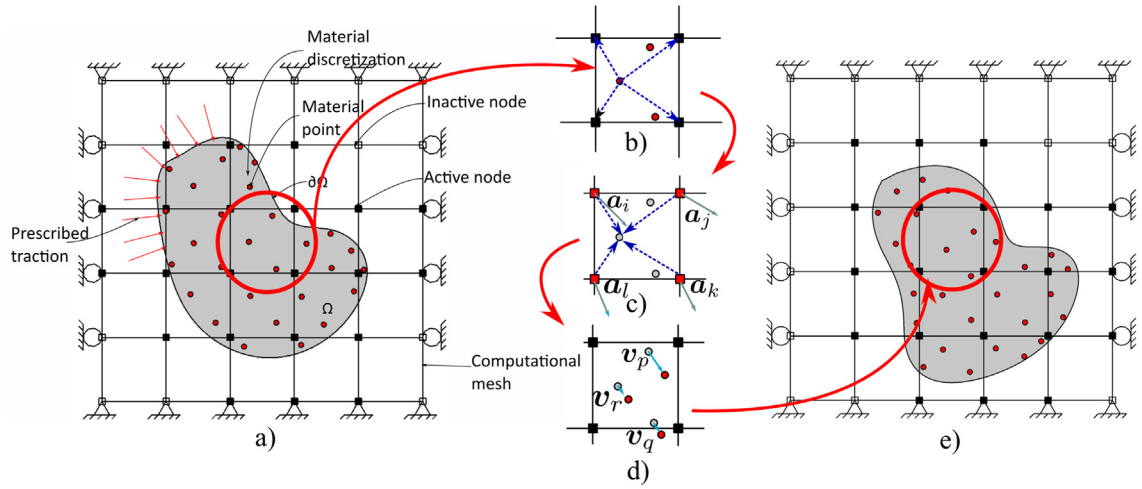

Fig. 1. MPM discretization and computational cycle: (a) initial configuration, (b) mapping from the material points to the nodes, (c) resolution of equilibrium equations in the computational grid (Lagrangian phase), (d) information transfer back to the material points, material points position is updated, and mesh data is discarded (convective phase), (e) deformed configuration.

and Alonso (2011) and Yerro et al. (2015), who proposed multi-phase approaches for the simulation of porous media under saturated or partially saturated conditions, respectively.

The capabilities of MPM for modeling impact were demonstrated by Sulsky et al. (1995) who presented a simulation of an elastoplastic rod at high velocity, and a rigid ball penetration into a strength-hardening aluminum target. Additional examples of the use of MPM for impact problems are the simulation of penetration trauma in biological soft tissues (Ionescu et al., 2005), the hyper-velocity impact of bullets and ballistic projectiles into metallic targets (Zhang et al., 2006; Huang et al., 2011), the impact of footings on porous media (Zhang et al., 2009), and the dynamic effects of projectile impacting on reinforced concrete structures (Lian et al., 2011). In the geotechnical field, MPM has also been applied to study impact and penetration problems. Al-Kafaji (2013) simulated a dynamic anchor installation into clay with a fully explicit dynamic MPM and the Mohr-Coulomb constitutive model. Phuong et al. (2016) simulated the installation of driven piles by means of a three-dimensional axisymmetric explicit MPM in sands with considerations of density changes. Ceccato et al. (2016a) and Ceccato et al. (2016b) evaluated the role of drainage conditions on the excess pore pressure produced by Cone Penetration Testing (CPT). More recently, Tran et al. (2017) and Tran and So lowski (2019) used the Generalized MPM (GIMP) (Bardenhagen and Kober, 2004) to simulate fall-cone test on normally consolidated sensitive clay.

The work presented below is performed with an internal version of the Anura3D MPM software (http://www.mpm-dredge.eu). This is a fully dynamic explicit MPM code that considers low-order elements (Fern et al., 2019). Hence, a first-order accuracy of the velocity field is expected. However, the solution is also affected by other factors such as the element size and the number of material points per element (Buzzi et al., 2008) or the updated stress procedure (Bardenhagen, 2002; Wallstedt and Guilkey, 2008). Moreover, the grid-crossing error reduces the accuracy of the simulation. Anura3D incorporates an MPM-mixed integration scheme (Al-Kafaji, 2013) to minimize this issue. Finally, the stability of the explicit scheme is ensured by fulfilling the Courant, Friedrichs, and Lewy (CFL) stability condition (Courant et al., 1967).

3. Physical experiment

3.1. Experimental setup

Controlled experiments have been performed at Virginia Tech by Albatal (2018), in which a BlueDrop FFP device (http://bluecdesigns.com) was dropped from a controlled height (h_d) in a cylindrical chamber filled with sand

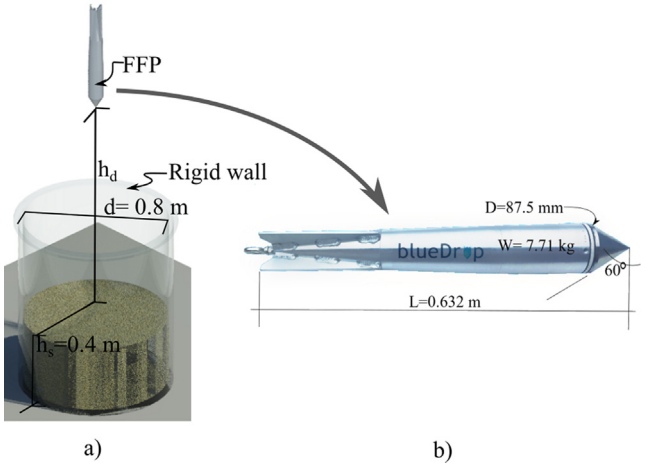

Fig. 2. (a) Experimental setup sketch, the cylinder is transparent only for illustration purposes. (b) BlueDrop FFP device. Retrieved and modified from http://bluecdesigns.com.

(Fig. 2). The sand in the chamber had 0.8 m of diameter and 0.4 m of height. Four accelerometers were installed in the FFP device to measure deceleration during penetration (Albatal, 2018). The sand was deposited, dropping the material without any additional vibration, procuring to obtain a loose relative density configuration. FFP's geometrical characteristics are shown in Fig. 2b. This study focuses on the experiments performed in dry sands.

3.2. Material properties

The tests were conducted on uniform sand from Yakutat, Alaska, using a triaxial vacuum test (VT) (Albatal, 2018). The tests were performed at low confining pressures, to match the in-situ stresses of shallow sediments, and at different initial void ratios. The experimental FFP testing was conducted on dry and loosely dropped sand. Thus, the relative density (D_r) is estimated to be near the loosest state (D_r = 0–15%). The results from the most representative triaxial testing are shown in Fig. 3. The sand dry unit weight (γ_d) is considered 14.6 kN/m^3 for a relative density of 0%. The peak internal friction angle ($\phi_p^{'}$) is determined to be around 38° to 40° and the critical friction angle ($\phi_c^{'}$) is determined to be 32°. The elasticity modulus (E') for a confining stress of 1.72 kPa (equivalent to 10.5 cm deep) is between 1000 and 5000 kPa for a D_r = 0–15% respectively, the coefficient of earth pressure at rest (K_0) is estimated using Jaky (1944) for $\phi^{'}$ = 38°, and the Poisson's ratio (ν') can be assumed to be 0.33. Table 1 summarizes the sand properties for a loose state.

The materials composing the BlueDrop FFP are mainly steel and aluminum, which have an elastic Young's modulus of approximately 200 × 10^6 kPa and 70 × 10^6 kPa respectively. This is up to 200,000 times higher than the sand Young's modulus.

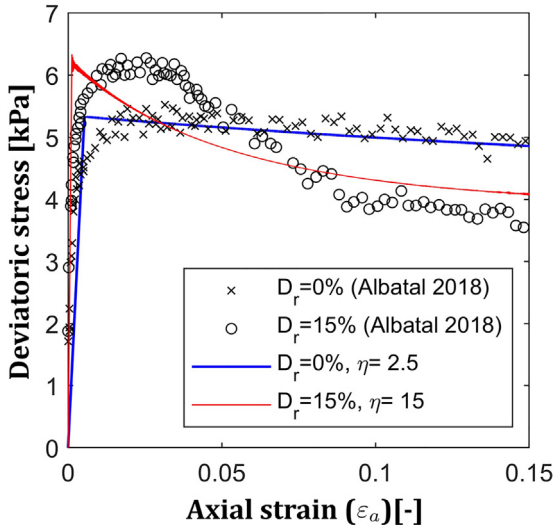

Fig. 3. Deviatoric stress vs. axial strain triaxial test with σ_3 = 1.72 kPa (data is taken from Albatal (2018)). Two curves from numerical triaxial testing, using the SSMC for calibration factors of 2.5 (blue line) and 15 (red line), are shown.

Table 1
Material properties for the sand at relative density between 0% and 15%.

Property	Value
Young's modulus (E') [kPa]	1000–5000
Poisson's ratio (ν') [–]	0.33
Peak friction angle ($\phi_p^{'}$)[°]	38–40
Critical friction angle ($\phi_c^{'}$)[°]	32
Cohesion (c') [kPa]	0
Coefficient of earth pressure at rest (K_0) [–]	0.39

3.3. FFP-soil contact properties

Durgunoglu and Mitchell (1973) have shown that the contact friction angle between sand and FFP (δ) can be expressed depending on the soil friction angle as $\delta = a\phi^{'}$, in which a is a factor that depends on the confining stress, the relative density of the soil, and the roughness of the devices surface. Durgunoglu and Mitchell (1973) reported values of a ranging between 0.28 and 0.90, being 0.28 the factor for polished aluminum and 0.9 the factor for sanded aluminum. Based on that, Albatal (2018) estimated that the contact friction angle between the BlueDrop FFP and the sand was approximately $\delta = 0.5\phi^{'}$, which is approximately δ = 20°.

4. Numerical model

The geometry of the model is defined by taking advantage of the symmetry of the experimental tests, hence a 20° slice of 1.1 m height and 0.4 m radius is considered (Fig. 4). The dimensions are consistent with the physical experiment setup (Fig. 2a). The FFP device consists of a 60° cone tip connected to a conic body with a total body mass of 7.71 kg. The outer edge has been slightly rounded to reduce numerical singularities (Fig. 4d). The cone is placed in immediate contact with the soil and based on physical experiments a 5.6 m/s initial impact velocity is assigned to the FFP device.

A four-nodded tetrahedral mesh is used to discretize the model. Since the accuracy of MPM improves with finer element size (Buzzi et al., 2008), the minimum element size (1 cm) is assigned around and below the cone tip. This distribution was found to optimize computational resources while giving accurate discretization of the FFP-soil contact surface (Fig. 4d).

One material point per element is assigned to the FFP (blue zone in Fig. 4a), ten material points are initially distributed in the elements representing the soil below the FFP (red zone in Fig. 4a), while four material points are considered for the soil closer to the boundary and more distant from the penetration zone (green zone in Fig. 4a). The total number of material points is 177,112. The fixities applied to the background mesh are indicated in Fig. 4b

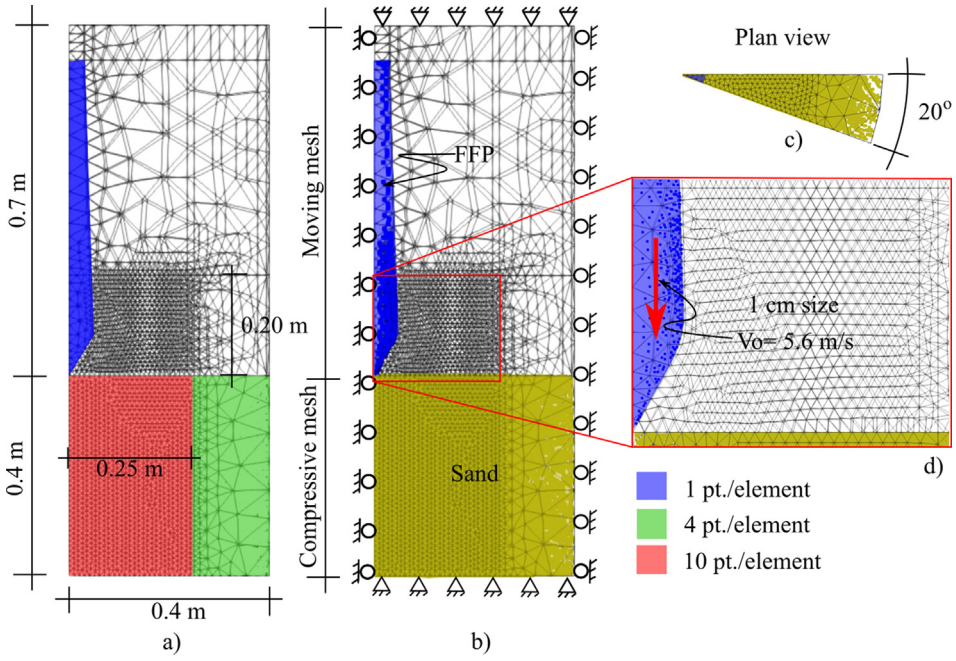

Fig. 4. Numerical model geometry configuration, mesh, and boundary conditions. (a) Dimensions and number of material points per element. (b) Moving mesh definition, material assignation, and schematic boundary conditions. (c) Model plan view which consist of a 20° cylinder. (d) Mesh refinement detail around the FFP tip. The minimum element size is 1 cm.

and ensure axisymmetric conditions; the bottom and top are fully fixed while other boundaries only allow free vertical displacements. A moving mesh technique (Al-Kafaji, 2013) is used to ensure that the FFP geometry remains well-defined throughout the penetration. This technique consists of subdividing the background computational mesh into a moving mesh and a compressing mesh (Fig. 4b). While the moving part moves following a reference material, in this case, the FFP, the remaining part compresses at the same rate. In this manner, the material points from the FFP stay inside their original elements throughout the simulation while keeping a well-defined contact surface (Ceccato et al., 2016a,b; Phuong et al., 2016).

This study employs the contact algorithm proposed by Bardenhagen et al. (2000), and the modifications recommended in Bardenhagen et al. (2001) to overcome unrealistic velocities that arise occasionally at the FFP tip. Bardenhagen et al. (2001) utilize a velocity scaling factor to rectify the contact velocity. In this study a scale factor of 0.75 is used.

A fully dynamic MPM formulation is considered, a strain-smoothing algorithm is used to mitigate volumetric locking (Al-Kafaji, 2013; Yerro, 2015), and a K_0 procedure ($K_0 = 0.39$) is employed to initialize the stresses. Artificial damping is not applied to account for the dynamic nature of the problem.

4.1. Rigid body algorithm

The formulation considered in this analysis is explicit, and as a result, it is conditionally stable. The stability condition (i.e., critical time step) for one-phase analysis (i.e., dry soil) follows the CFL condition (Courant et al., 1967), which depends on the bulk modulus of the material into consideration. The larger the elastic modulus, the lower the critical time step. Therefore, the computational cost of the model proposed in this analysis directly depends on the bulk modulus of the FFP material (about to 200,000 times higher than the modulus of sand). In order to optimize the computational resources, a rigid body algorithm is proposed, which consists of performing the calculation independently of the FFP modulus by means of assuming that the FFP device is incompressible (i.e., moves as a solid-rigid). In this way, the stability criterion only depends on the bulk modulus of the soil and the calculation time is minimized.

The rigid body algorithm is embedded into the moving mesh framework and can work together with the contact algorithm. The proposed algorithm consists of the following steps which are also illustrated in Fig. 5:

(1) In the Lagrangian phase, the nodes at the contact between the rigid body and surrounding material are identified (Fig. 6), the sum of internal and external forces is balanced with the rate of momentum, and the acceleration of the rigid body is obtained as the ratio between the rate of moment and its total mass as follows:

$$\boldsymbol{a}_{rb} = \frac{\left(m_{rb}\boldsymbol{g} + \boldsymbol{t}_{rb} - \sum_{i=1}^{n_c} \boldsymbol{f}^{i}_{soil}\right)}{m_{rb}} \tag{1}$$

where $\boldsymbol{a}_{rb}$ is the acceleration vector of the rigid body, m_{rb} is the total mass of the rigid body, $\boldsymbol{g}$ is the gravity acceleration vector, $\boldsymbol{t}_{rb}$ is the external load vector

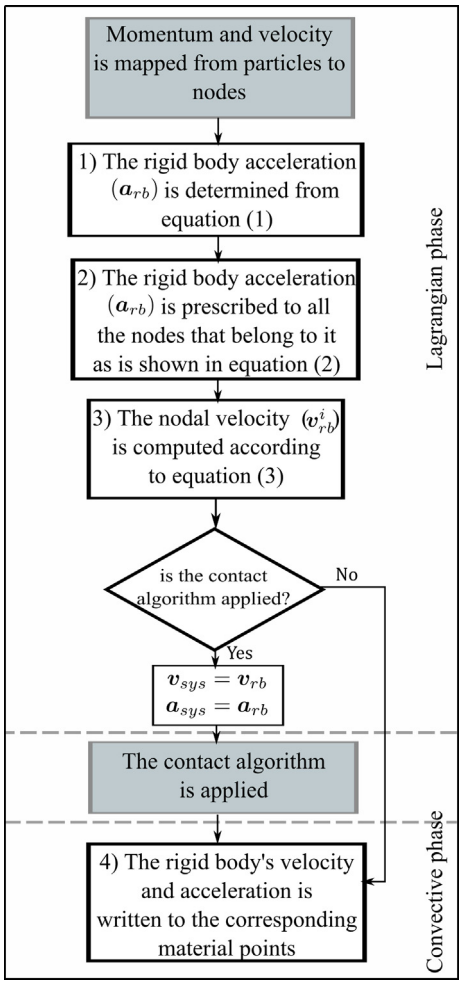

Fig. 5. Rigid body algorithm flow diagram. The shaded rectangles are processes that run independently of the rigid body algorithm. MPM phases and the contact algorithm are included for reference.

applied to the rigid body (equal to 0 for this study), n_c is the number of nodes within the contact surface (see Fig. 6), i is the node relative index within the contact surface. Finally, f^i_{soil} is the force transmitted from the soil to the FFP at the $i-$ th contact node, which is calculated as the $i-$ th nodal internal force only considering the contribution from soil material points. Note that the model analyzed in this work is axisymmetric around the FFP axis; hence, only the vertical component of the reaction force is required.

(2) At the end of the Lagrangian phase, the nodal acceleration of the rigid body (a^i_{rb}) is updated based on the acceleration of the rigid body calculated in the previous step (a_{rb}):

$$a^i_{rb} = a_{rb} \quad for: \quad 1 \le i \le n_{rb} \tag{2}$$

where i denotes the node number within a total of n_{rb} nodes (blue and red zone in Fig. 6)

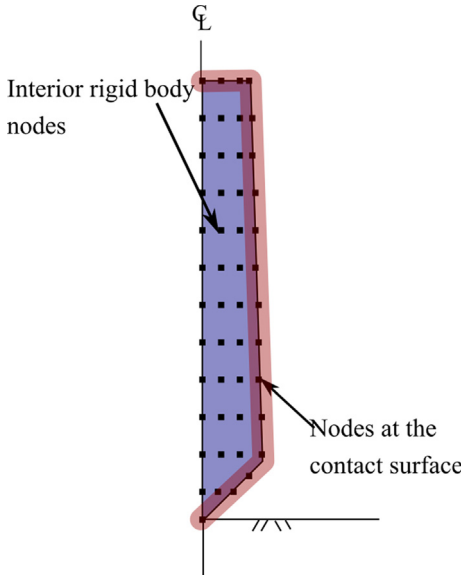

Fig. 6. Nodes belonging to the FFP (blue and red zone), and nodes belonging to the contact surface (red zone).

(3) The nodal velocity of the rigid body (v^i_{rb}) is calculated as:

$$v^i_{rb} = v^i_0 + a^i_{rb}\Delta t \quad for: \quad 1 \le i \le n_{rb} \tag{3}$$

with v^i_0 being the velocity at the beginning of each time-step, a^i_{rb} is the current nodal acceleration, and Δt is the time-step increment. Note that in this manner, the rigid motion is ensured in all the nodes of the rigid body.

(4) During the convective phase, the velocity and acceleration of the material points in the rigid body are updated based on the nodal values. Finally, the position of the material points is updated accordingly.

In this paper, the rigid body algorithm is used together with the contact algorithm proposed by Bardenhagen et al. (2001). To account for relative displacement and free separation of different bodies, the contact algorithm requires the evaluation of different acceleration and velocity fields at the nodes: one for each body (v_{soil}, a_{soil}, v_{rb}, and a_{rb}) and one for the system (v_{sys}, a_{sys}) (i.e., combined body fields) (Bardenhagen et al., 2001). In order to ensure that the contact algorithm is compatible with the rigid body motion, the acceleration and velocity obtained in steps 2 and 3 must be prescribed to the system (i.e., $v_{sys} = v_{rb}$ and $a_{sys} = a_{rb}$) before the contact algorithm is applied (Fig. 5).

Note that the rigid body algorithm proposed here is only valid for rigid body linear motions since we only consider the linear momentum balance. This could be extended to simulate rigid body rotation by solving the angular momentum.

4.2. Modeling of sand constitutive behavior

The behavior of sands in static conditions has been extensively studied for decades. In particular, the sand considered in this analysis was characterized by quasi-static laboratory testing (Section 3.2). Fig. 3 shows the results from a vacuum triaxial performed on two dry specimens with a relative density of 0% and 15%. It is clear from Fig. 3, that the strength slightly decreases after reaching a peak value indicating a strain-softening behavior. The results for different confinements and relative densities, published by Albatal (2018), also indicate a behavior dominated by dilatancy, after which the softening process takes place.

The effects of HSR were not studied for the sand considered in this experimental analysis, but data from other authors has been analyzed for reference. The effects of HSR in the constitutive behavior of sands have been studied using fast vacuum triaxial testing on crushed coral sands (Yamamuro et al., 2011) and quarzitic sands (Suescun-Florez et al., 2015). It is observed that the peak friction angle increases with the strain-rate effects. This hardening process occurs until, eventually, under a certain deformation, a softening process takes place while the dilatancy varies (i.e., transient dilatancy). Additionally, as the strain rate increases, the sand experiences less contraction and the dilatancy behavior is more dominant. This last effect has also been recognized by (Omidvar et al., 2012 and Barr, 2016). Consistently, almost all sand specimens tested by Yamamuro et al. (2011) experienced strain localization due to softening; however, there was no clear evidence regarding the effects of HSR on the dilatancy angle. The effect of HSR in the sand's Young's modulus has also been reported by several authors (Seed and Lungren, 1954; Yamamuro et al., 2011; Omidvar et al., 2012; Barr, 2016), and an increase up to 115% has been observed for the range of strain rates in which the FFP operates.

In this study, two constitutive models are considered to simulate the behavior of sand during FFP penetration: a non-associate Mohr-Coulomb constitutive model (MC), and a Strain-Softening Mohr-Coulomb (SSMC) model. In any case, the material is assumed to be dry, and the air in the porous is supposed to be fully drained. Material parameters showed in Table 1 are used for reference. First, the MC model is used, to evaluate the effects of the elastic bulk modulus of sand and the FFP-sand contact friction angle. Secondly, the SSMC model is taken into account to study the effect of transient dilatancy, strain-softening effect, observed in quasi-static conditions, and the effects of larger peak friction angles associated with HSR effects. The motivation for the use of MC and SSMC to simulate the sand behavior is mainly because of their simplicity. They allow to have a first understanding of the aspects of HSR in sands, at the same time that the MPM framework is tested to model high-velocity impact soil-structure problems.

The peak dilatancy angle has been correlated with the relative density (D_r) using Bolton (1986) equation, which is given by:

$$D_{max} = 0.3 I_R \tag{4}$$

where D_{max} is a proxy for the tangent of the maximum dilatancy angle (Fern et al., 2016), and I_R is the relative dilatancy index defined by:

$$I_R = D_r(10 - \ln(p'[\text{kPa}]) - 1 \tag{5}$$

For the sand considered in this analysis, dilatancy angles in the range of 0° to 10° are obtained with a combination of mean effective stresses between 1 kPa and 3 kPa (0 m to 0.2 m of penetration depth), and relative densities between 0% and 15%.

Finally, the SSMC requires a calibration factor (η) that controls the decrease of shear strength rate with accumulated plastic deviatoric strain (Yerro, 2015, Yerro et al., 2016). The calibration procedure is performed by running a set of triaxial numerical simulations on weightless models. The dimension of the reference numerical test is equivalent to the soil specimen employed in the laboratory (0.15 m high and 0.07 m of width) (Albatal, 2018). The numerical specimen is discretized using elements of the same size as those considered in the FFP model (1 cm). In this context, η is adjusted to fit the laboratory results for the two reference relative densities near the loosest state (0% and 15%) (Fig. 3). The fitting method is based on the smeared crack approach theory (Rots et al., 1985), which consists in ensuring that the total dissipated work in the numerical model and in the laboratory experiment are the same. In practice, this means that the area below the displacement vs force curve obtained in the numerical analysis must be equivalent to the one obtained from the laboratory. Following this procedure, it is possible to reduce the mesh dependency problems that arise due to the inclusion of strain-softening features (Soga et al., 2015). From Fig. 3, it is important to note that since the rate of strength decrease varies depending on the relative density, different η values are obtained for each triaxial test.

5. Numerical results

Several numerical analyses have been performed to study the effect of the most relevant variables in the FFP penetration. First, the FFP compressibility and the effectiveness of the solid-rigid body algorithm are analyzed; secondly, the effect of the soil's elasticity is investigated; and third, the effect of the FFP-soil contact friction angle is presented. In these analyses, the MC constitutive model, without dilatancy, has been used to model the behavior of the sand. Afterward, the contribution of the dilatancy is evaluated. Finally, the strain-softening behavior of the sand is incorporated by means of an SSMC model and the peak friction angle is increased to evaluate the HSR effects in the problem. The numerical results are compared with the experimental data.

5.1. Effect of the FFP compressibility

The effect of the FFP compressibility is analyzed by comparing the results of two simulations. The first model considers the FFP as an incompressible device using the rigid body algorithm proposed in Section 4.1, while in the second simulation, the FFP is modeled as a linear-elastic body with a Young's modulus of $E = 20{,}000$ kPa and a Poisson's ratio of $\nu = 0$. In both cases, the rest of the parameters are identical and consistent with those measured in the laboratory (Section 3.1). The FFP-soil contact friction angle is $\delta = 20°$, and the sand is simulated with the MC constitutive equation, with $\phi' = 39°$, $\nu' = 0.33$, and $E' = 2{,}500$ kPa.

Fig. 7 shows the time-histories for the penetration depth (Fig. 7a), velocity (Fig. 7b), and deceleration (Fig. 7c) of one representative material point located at the center of the FFP. The reaction force at the cone boundary is also plotted in Fig. 7d. In general, the results from both models are very consistent, which validate the implementation of the rigid body algorithm. The model that considers a compressible FFP presents oscillations, especially in the deceleration process. This is because the FFP can deform and vibrates due to the dynamics of the problem. However, the trend of the elastic solution is in good agreement with the solution with the rigid body, in which the noise is canceled. The reaction forces (Fig. 7d) are also consistent. The reaction increases until a maximum value is recorded at $t \approx 0.03$ s, then, it slowly decreases until $t \approx 0.06$ s. After this, the reaction drastically decreases. From $t \approx 0.07$ s to $t \approx 0.11$ s, the FFP slightly bounces back, and because the contact algorithm allows free separation, the reaction force is consistently zero. Finally, at $t \approx 0.12$ s, the FFP stabilizes, and the reaction force approaches the FFP weight (i.e., 0.075 kN).

Apart from getting a more stable solution, another advantage of simulating the FFP as a rigid body is that the computational time decreases by 57% (from 14 to 6 h with an Intel Core i7 at 2.6 GHz CPU) (Zambrano-Cruzatty and Yerro, 2019). The reasons for the time reduction are i) the critical time step is increased, and ii) there is not a constitutive behavior associated with the FFP solid-rigid body; hence, the stress updating algorithm at these material points is avoided. The FFP models presented hereafter are all performed with the rigid body algorithm.

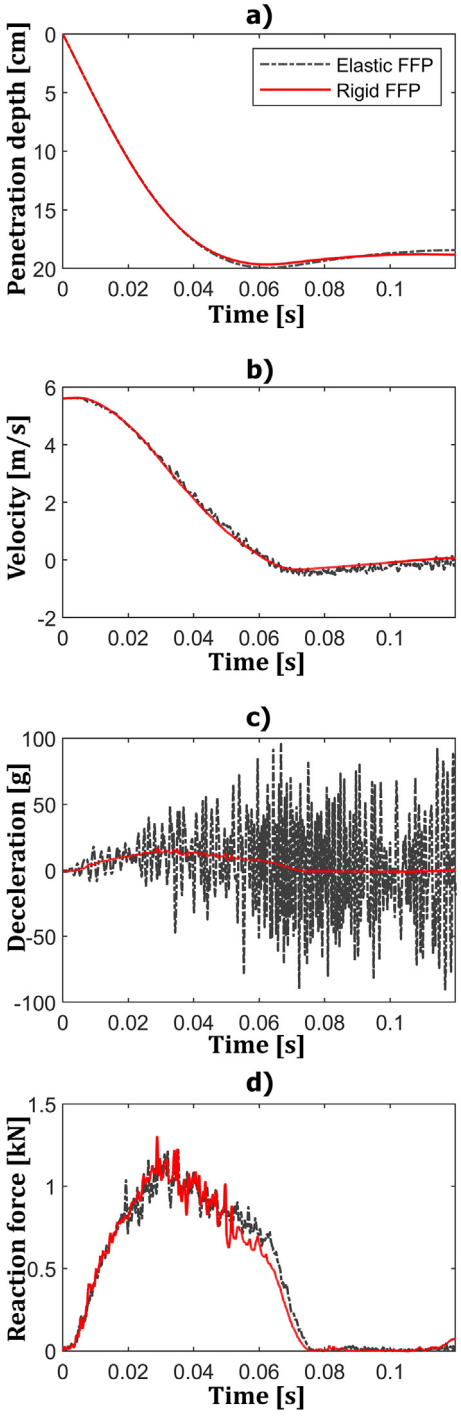

Fig. 7. Effects of simulating the FFP as a linear-elastic or a solid-rigid body. (a) Penetration depth vs. time, (b) velocity vs. time, (c) deceleration vs. time, and (d) reaction force vs. time.

5.2. Effect of the Young's modulus of the sand

In this study, the influence of the soil's elasticity is analyzed by considering five models with Young's modulus of $E' = 1{,}000$ kPa, $E' = 2500$ kPa, $E' = 5000$ kPa, $E' = 7500$ kPa, and $E' = 10{,}000$ kPa. Note that 1,000 kPa and 5,000 kPa correspond to the quasi-static elasticity modulus obtained for a relative density of 0% and 15%, respectively, for a confinement equivalent to 10.5 cm deep. In all cases the MC model is considered with $\phi' = 39°$and $\nu' = 0.33$, and the contact friction angle is $\delta = 20°$.

Fig. 8a shows the penetration time-history of the FFP. Although the final penetration depth appears to be not affected by the sand stiffness (ranges from 18 to 20 cm) (Fig. 8a), a substantial difference can be detected in the velocity and deceleration profiles between the different models (Fig. 8 b and c). Those models with stiffer sands

(i.e., $E' = 5{,}000$ kPa, $E' = 7{,}500$ kPa, and $E' = 10{,}000$ kPa) present a velocity profile almost identical which fits the experimental data at low penetration depths, however they present a curved profile for larger penetration depths. Contrarily, the numerical solution with $E' = 1{,}000$ kPa generally overestimates the magnitude of the velocity, and at the end of the penetration, it becomes negative while the FFP bounces back (Fig. 8b) which have not been observed in the physical experiments. The deceleration profiles (Fig. 8c) also indicate a very similar trend for the stiffer materials: a main peak is presented in shallow depths (as the stiffness increases the peak is shallower) and a secondary peak appears later in the penetration (around 16 cm deep). On the contrary, in the softer model, the deceleration increases until near the end of the simulation, when suddenly decreases. In all models, the magnitude of the maximum deceleration is essentially constant, around 15 g, which underestimates the experimental results by 21%. Accordingly, the final penetration is also overestimated (by 25%).

In Fig. 9 the deviatoric strain contour plots for three simulations ($E' = 1{,}000$ kPa, $E' = 2{,}500$ kPa, and $E' = 5{,}000$ kPa) at $t = 0.04$ s and $t = 0.06$ s are shown (the secondary peak develops within this time lap). A "general" bearing capacity failure mechanism is fully developed and connects to the ground surface for the stiffer model ($E' = 5{,}000$ kPa) (Fig. 9c). The same behavior is observed in all the simulations with stiffer sands ($E' = 7{,}500$ kPa, and $E' = 10{,}000$ kPa) and is a clear indication that the occurrence of a secondary peak in the deceleration profile is related to the development of a general failure mechanism. Once the failure surface is formed and a kinematically unstable wedge is created, the confinement around the FFP is reduced which modifies the kinematic behavior of the system. Contrarily, when $E' = 1{,}000$ kPa (Fig. 9a), a "punching" type of failure is observed, and there is no further development of any shear band localization. In this situation, the deformation is more widespread. Finally, when $E' = 2{,}500$ kPa (Fig. 9b), the failure mechanism type is "localized", which means that the deformations are concentrated in the zones where the shear bands are forming, but the failure mechanism does not reach the surface. All these mechanisms are consistent with reported bearing capacity failure types in sands, which demonstrated that the sand compressibility controls the failure mode (Vesic, 1973; Salgado, 2008).

For further simulations, a Young's modulus of $E' = 2{,}500$ kPa has been considered because, in general, the numerical results describe a similar behavior to the experimental data (only one deceleration peak is observed), and it is reasonable taking into account the modulus obtained with laboratory data for loose sand.

5.3. Effect of the contact friction angle

A parametric analysis has been carried out to study the effect of the contact friction angle between FFP and soil (δ). Based on the literature (Durgunoglu and Mitchell, 1973; Albatal, 2018), a range of contact friction angles has been evaluated (from $\delta = 20°$ to fully rough conditions). The sand properties are identical to those presented in Section 5.1.

Fig. 10 shows the penetration time-history (Fig. 10a), the velocity profile (Fig. 10b), and the deceleration profile (Fig. 10c). It can be observed that higher values of δ result in a lower penetration depth and a tendency to bounce back. In terms of velocity, it can be seen that when the contact is fully rough the numerical and the experimental solution are in good agreement.

The deceleration profile obtained with the MPM results is comparable to the experimental deceleration profile shown by the blue dashed line (Fig. 10c). As the contact friction angle increases, the peak deceleration also increases. The maximum deceleration obtained from MPM ranges between 15 g and 19 g, which are relatively in good agreement with the experimental value (i.e.,

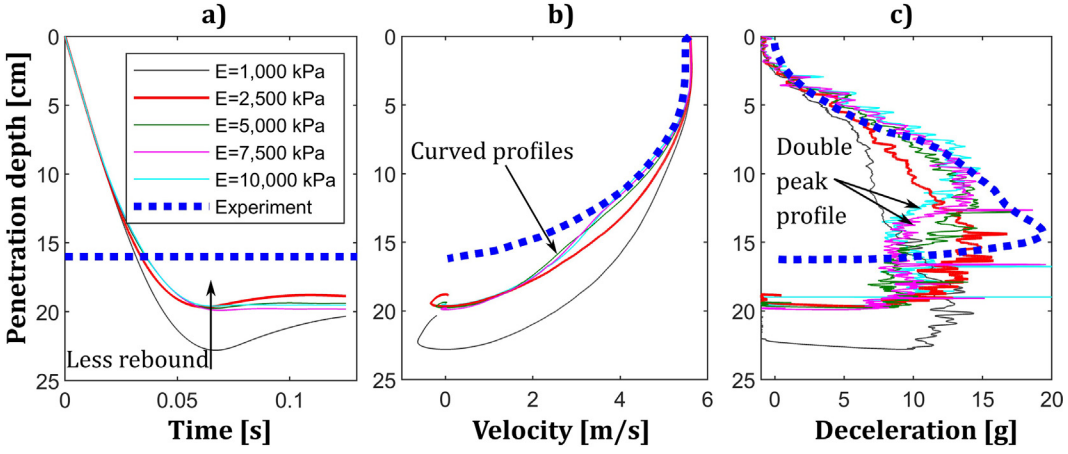

Fig. 8. Effect of the sand stiffness in the numerical solution compared to the experimental results. (a) Penetration time-history, (b) velocity profile, (c) deceleration profile.

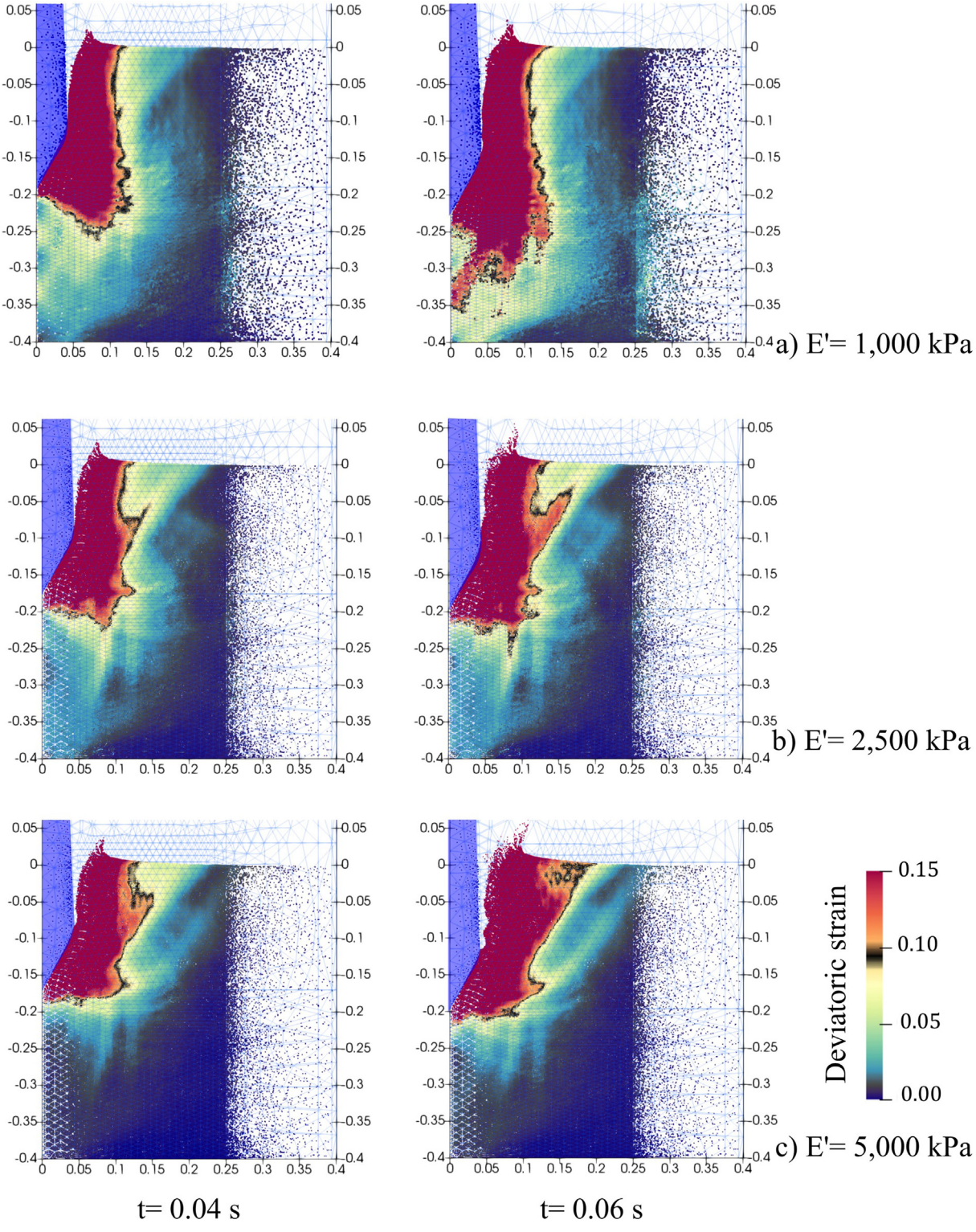

Fig. 9. Deviatoric strain contour plots at $t = 0.04$ s and $t = 0.06$ s for (a) E' =1,000 kPa, (b) E' =2,500 kPa, and (c) E' =5,000 kPa.

19.4 g). Although a better approximation between the numerical results and the experiments is achieved by the solution with fully rough contact, it is not reasonable to neglect the sliding contact behavior of the FFP-soil interaction. Moreover, the final penetration depth requires refinement to eliminate the excessive bouncing. The solution with $\delta = 20°$ produces a more realistic penetration behavior (less rebound) and it seems reasonable based on experimental data (Albatal, 2018). Therefore, $\delta = 20°$ is selected for posterior analysis.

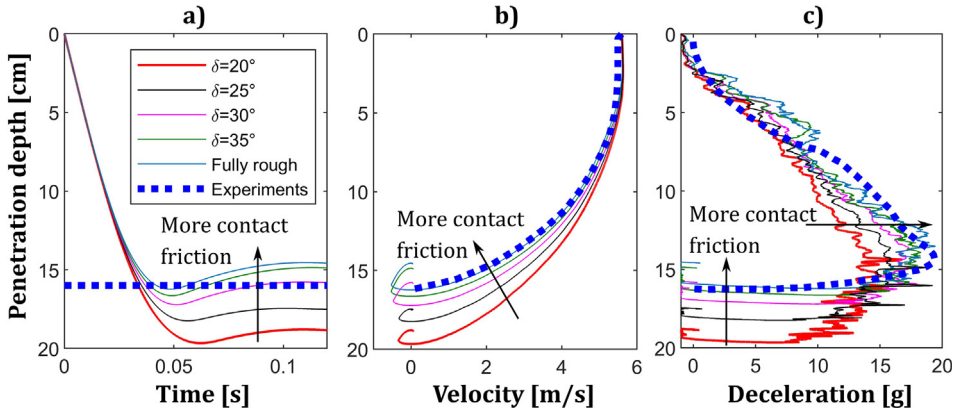

Fig. 10. Effect of the contact friction angle on the penetration depth (a), velocity (b), and deceleration (c). The experimental results are presented for reference.

5.4. Effect of the dilatancy

Taking into account the range of dilatancy obtained in Section 4.2, five models have been analyzed considering a transient reduction of β, from a peak value (β_p = 2.5°, 5°, 7.5°, 10°) down to 0° as a function of the plastic deviatoric strain. The SSMC constitutive equation is used with $\phi_p^{'} = 39^{\circ}$, $\phi_c^{'} = 39^{\circ}$,500 kPa, and $\nu' = 0.33$. For all cases the calibration parameter (η) is set to 8°, which gives an intermediate strain-stress response for loose sand (D_r = 0–15%). The contact friction angles is $\delta = 20°$.

The numerical results are presented in Fig. 11. As β increases, the FFP bounce back at the end of the penetration decreases (Fig. 11a). However, the final penetration depth remains unaffected by the dilatancy because β vanishes for large deformations. The velocity profile (Fig. 11b) appears to be more affected because it evolves from a singled curvature profile to a curved profile. In terms of deceleration (Fig. 11c), it can be seen that for higher dilatancy angles, the maximum deceleration increases slightly.

In further simulations, a transient dilatancy with $\beta_p = 5°$ has been considered for reference because it has a reduced rebound while keeping a single curvature velocity profile.

5.5. Effect of the peak friction angle

In this section the HSR effects described in 4.2 are considered by using the SSMC model and increasing the peak friction angle from $\phi_p^{'} = 39^{\circ}$ to $\phi_p^{'} = 60^{\circ}$. Based on Table 1, the critical friction angle is set to $\phi_c^{'} = 32^{\circ}$. The rest of the parameters are identical and consistent with the previous section.

Fig. 12 shows the effect of the peak friction angle for the simulations with $\phi_p^{'}$ = 39°, 46°, 50°, and 60° with remarkable results compared to the experiments. A clear reduction of the penetration depth is observed for larger peak friction angles (Fig. 12a). Moreover, the final penetration depth with SSMC is about 22% deeper than with MC for $\phi^{'}$ =39° (Fig. 10a), which is evidently an effect of the strain-softening behavior. A consistent outcome is

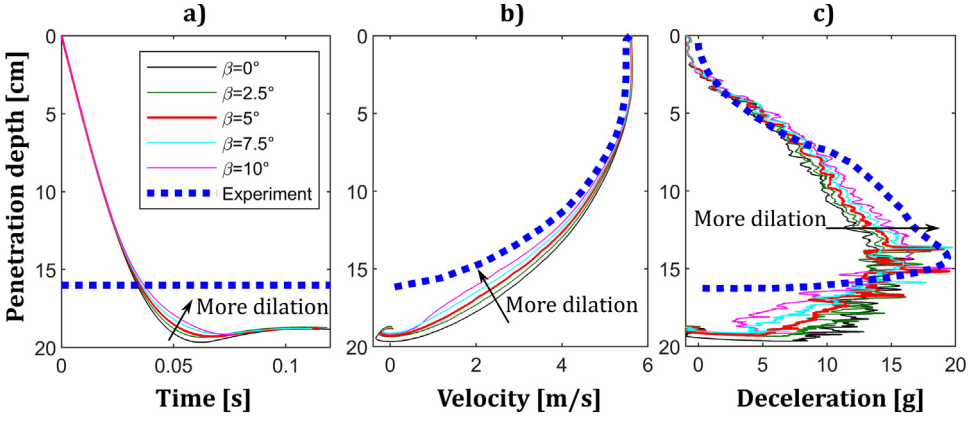

Fig. 11. Effect of the dilatancy angle in the penetration depth (a), velocity profile (b), and deceleration (b). The black arrows indicate the influence of increasing the dilatancy.

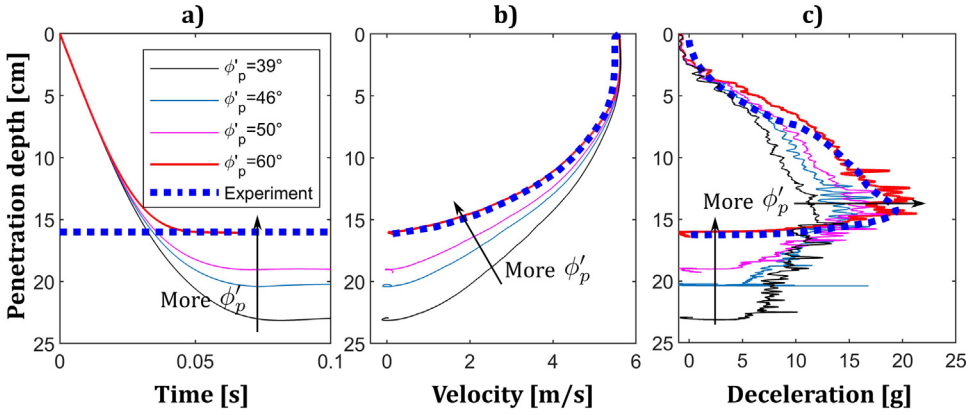

Fig. 12. Influence of the peak friction angle in the penetration (a), velocity (b), and deceleration (c). The black arrows indicate the effects of increasing the peak friction angle.

observed in the velocity profiles (Fig. 12b). Finally, when ϕ'_p increases, the peak deceleration increases and the behavior of the deceleration curve shows a sharper reduction and a longer plateau at the very last part of the penetration, matching the experimental results with an excellent agreement (12c).

Fig. 13 shows the final penetration depth and the maximum deceleration for the different peak friction angles. As described above, as the peak friction angle increases, the maximum deceleration increases, and the penetration depth decreases following a linear trend.

6. Discussion

The parametric analysis on the sand Young's modulus showed that when stiffness is relatively high ($E' >$ 5,000 kPa), a secondary peak is observed in the deceleration profile, which indicates the development of a general bearing capacity failure mechanism. When the stiffness is lower, only one deceleration peak is observed, and a local failure is developed. In practice, there is no evidence of the failure mode developed in FFP deployment, but the experimental deceleration profiles portrait a single peak. Based on the numerical results presented in this analysis, this would be consistent with a local mechanism. However, the procedures considered to correlate the material properties with FFP measurements rely on state limit analyses such as the Terzaghi's bearing capacity theory (Albatal, 2018). These assume the formation of a general bearing capacity failure mechanism. Further research should be considered to study the HSR effects on the failure mechanism by means of more advanced constitutive models. In particular, the HSR effect on the Young's modulus and the dilatancy angle, which are not considered in this study. Also, the influence of drainage conditions of the air filling the porous during the penetration could have an impact on the failure development and should be investigated. On the other hand, a $\phi'_p = 60^\circ$ is required to match the experiments.

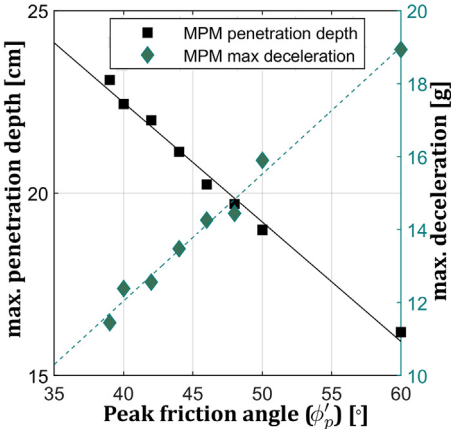

Fig. 13. Peak friction angle vs. final penetration depth [cm] (left axis) and maximum deceleration [g] (right axis).

This value is higher than the peak friction angle estimated in the laboratory under quasi-static conditions (ϕ'_p =38° to 40°). This fact can be explained by the HSR effects described in the literature (Section 4.2). In practice, the sediment properties are determined using empirical equations based on quasi-static testing (e.g. CPT). Since the FFP field data includes HSR, this data is filter-out to obtain the corresponding quasi-static reaction of the soil. A common methodology used to filter-out the effect of the HSR is presented in Equation (6) (Albatal, 2018), in which the reaction at the FFP tip obtained from field data (F_{dyn}) is related to the quasi-static tip reaction (F_0), the FFP velocity (v), and a reference velocity (v_{ref}) which is typically 2 cm/s (i.e., CPT testing rate). Finally, K is a fitting factor.

$$F_{dyn} = F_o\left(1 + K\log\left(\frac{v}{v_{ref}}\right)\right) \tag{6}$$

As an attempt to validate the methodology proposed in this numerical analysis, a K factor is estimated from the MPM model and compared with the range proposed by previous authors (K = 0.2–1.5) (Stoll et al., 2007; Stark

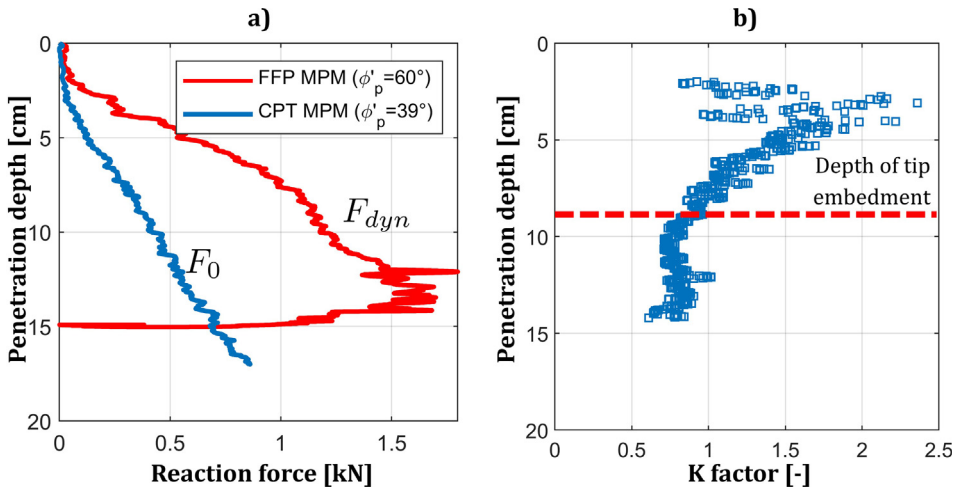

Fig. 14. (a) Dynamic (FFP) and static (CPT) reaction force profiles, (b) K factor profile.

et al., 2012; Albatal, 2018). The dynamic reaction force profile (F_{dyn}) is obtained from the calibrated model (Section 5.5). To determine the quasi-static $\phi'_p = 60^\circ$ reaction force profile (F_0), an additional quasi-static FFP penetration (CPT-like simulation) is performed, where the FFP velocity is prescribed constant ($v_{ref} = 2$ cm/s). For consistency, the peak friction angle in the quasi-static model is assumed 39° based on triaxial testing (Table 1). Both F_{dyn} and F_0 are presented in Fig. 14a. A K profile is determined by isolating the K factor from Equation (6) and considering the FFP velocity profile from Fig. 12b for the calibrated model. K values oscillate between 0.8 and 2.0 before the FFP tip is fully embedded, and after that, K remains approximately constant and equal to 0.75 (Fig. 14b). This range is in good agreement with the values reported in the literature (Stoll et al., 2007; Stark et al., 2012; Albatal, 2018), which validates the numerical results obtained with a $\phi'_p = 60^\circ$.

7. Conclusions

This study proposes a numerical framework capable of simulating FFP penetration in dry sands using MPM. It includes a moving mesh technique, attached to the FFP structure, to ensure a well-defined FFP geometry throughout the calculation. The soil-FFP interaction is modeled employing a frictional contact algorithm, and a rigid body algorithm is proposed to simulate the incompressibility of the FFP, reducing the computational effort.

The physical characteristics of an FFP penetration laboratory experiment as well as the geotechnical properties of the sand are presented. To study the effect of the most relevant variables in the FFP penetration, several parametric analyses are performed. The analysis of soil's elasticity and FFP-soil contact friction angle are considered by taking into account a Mohr-Coulomb constitutive model. It is found that sand stiffness has an important effect on the characteristics of the failure mechanism. In stiffer sands ($E' \geq 5{,}000$ kPa), a general bearing capacity failure is developed, which leads to a deceleration profile with two peaks. In softer materials, a "punching" or "local" failure mechanism is displayed, and a deceleration profile with a unique peak is exhibited. Moreover, as the stiffness increases, a lower bounce back is observed at the end of the penetration. Besides, when the FFP-soil contact friction angle increases, the maximum deceleration increases, the penetration depth reduces, and enhances the bouncing back effect. Based on the experimental tests used for reference, the values of $E' = 2{,}500$ kPa and $\delta = 20°$ present the most reasonable results.

The effects of dilatancy and HSR have been taken into account by using the strain-softening Mohr-Coulomb model. As the dilatancy angle decreases, the bouncing back increases, and the maximum deceleration slightly decreases. The effect of the dilatancy in the penetration depth is negligible. A value of 5° shows a realistic rebound, and it is in accordance with the estimated range of relatives densities considered in this analysis.

Based on studies presented by Yamamuro et al. (2011); Omidvar et al. (2012); Suescun-Florez et al. (2015), the effects of high strain-rates have been included by increasing the peak friction angle while maintaining the critical friction constant and equivalent to the quasi-static one. The penetration depth decreases linearly with the peak friction angle. Consistently, the peak deceleration increases linearly with the peak friction angle. The model considering a peak friction angle of $\phi'_p = 60^\circ$ fits the experimental results.

The results obtained in this work show that MPM can simulate FFP deployment in dry sands efficiently. Although simple constitutive models have been considered, the numerical results fit well with the experimental data. In any case, the implementation of more advanced constitutive models including rate effects, are required to improve the understanding of FFP deployment in sands.

Acknowledgements

The authors want to thank the collaboration of Dr. Nina Stark and Dennis Kiptoo for providing the experimental data for conducting this study.

References

Abelev, A., Tubbs, K., Valent, P., 2009. Numerical investigation of dynamic free-fall penetrometers in soft cohesive marine sediments using a finite difference approach, 1–10.

Al-Kafaji, I.K.J., 2013. Formulation of a Dynamic Material Point Method (MPM) for Geomechanical Problems. Ph.D. thesis. University of Stuttgart, Stuttgart.

Albatal, A., 2018. Advancement of using portable free fall penetrometers for geotechnical site characterization of energetic sandy nearshore areas. Ph.D. thesis. Virginia Polytechnic Institute and State University.

Albatal, A., Mcninch, J.E., Wadman, H., Stark, N., 2017. In-situ geotechnical investigation of nearshore sediments with regard to cross-shore morphodynamics. Geotech. Front. 2017, 398–408.

Aubeny, C.P., Shi, H., 2006. Interpretation of impact penetration measurements in soft clays. J. Geotech. Geoenviron. Eng. 132, 770–777.

Bardenhagen, S., 2002. Energy conservation error in the material point method for solid mechanics. J. Comput. Phys. 180, 383–403.

Bardenhagen, S.G., Brackbill, J.U., Sulsky, D., 2000. The material-point method for granular materials, 529–541.

Bardenhagen, S.G., Guilkey, J.E., Roessig, K.M., Brackbill, J.U., Witzel, W.M., Foster, J.C., 2001. An improved contact algorithm for the material point method and application to stress propagation in granular material. CMES – Comput. Model. Eng. Sci. 2, 509–522.

Bardenhagen, S.G., Kober, E.M., 2004. The generalized interpolation material point method. Comput. Model. Eng. Sci. 5, 477–495.

Barr, A.D., 2016. Strain-Rate Effects in Quartz Sand. Ph.D. thesis. University of Sheffield.

Bolton, M.D., 1986. The strength and dilatancy of sands. G´eotechnique 36, 65–78.

Buzzi, O., Pedroso, D.M., Giacomini, A., 2008. Caveats on the implementation of the generalized material point method. Comput. Model. Eng. Sci. 31, 85–106.

Carter, J.P., Nazem, M., Airey, D.W., Chow, S.H., 2010. Dynamic analysis of free-falling penetrometers in soil deposits. In: GeoFlorida 2010: Advances in Analysis, Modeling & Design, pp. 53–68.

Ceccato, F., Beuth, L., Simonini, P., 2016a. Analysis of piezocone penetration under different drainage conditions with the two-phase material point method. J. Geotech. Geoenviron. Eng. 142, 04016066.

Ceccato, F., Beuth, L., Vermeer, P.A., Simonini, P., 2016b. Two-phase Material Point Method applied to the study of cone penetration. Comput. Geotech. 80, 440–452.

Courant, R., Friedrichs, K., Lewy, H., 1967. On the partial difference equations of mathematical physics. IBM J. Res. Dev. 11, 215–234.

Durgunoglu, H., Mitchell, J.K., 1973. Static Penetration Resistance of Soils Technical Report. Space Sciences Laboratory, Berkeley, CA.

Fern, E.J., Robert, D.J., Soga, K., 2016. Modeling the stress-dilatancy relationship of unsaturated silica sand in triaxial compression tests. J. Geotech. Geoenviron. Eng. 142, 04016055.

Fern, J., Rohe, A., Soga, K., Alonso, E., 2019. The Material Point Method for Geotechnical Engineering: A Practical Guide. CRC Press.

Huang, P., Zhang, X., Ma, S., Huang, X., 2011. Contact algorithms for the material point method in impact and penetration simulation. Int. J. Numer. Meth. Eng. 85, 498–517.

Ionescu, I., Guilkey, J., Berzins, M., Kirby, R.M., Weiss, J., 2005. Computational simulation of penetrating trauma in biological soft tissues using the material point method. Medicine Meets Virtual Reality 13: the Magical Next Becomes the Medical Now 111, 213–218.

Jaky, J., 1944. The coefficient of earth pressure at rest. J. Soc. Hungarian Architects Eng., 355–358.

Kim, Y.H., Hossain, M.S., Wang, D., Randolph, M.F., 2015. Numerical investigation of dynamic installation of torpedo anchors in clay. Ocean Eng. 108, 820–832.

Lian, Y.P., Zhang, X., Zhou, X., Ma, Z.T., 2011. A FEMP method and its application in modeling dynamic response of reinforced concrete subjected to impact loading. Comput. Methods Appl. Mech. Eng. 200, 1659–1670.

Liu, X.D., Sun, J., Yi, J.T., Lee, F.H., Gu, H., Chow, Y.K., 2014. Physical and numerical modeling of the performance of dynamically installed anchors in clay. In: Proceedings of the ASME 2014 33rd International Conference on Ocean, Offshore and Arctic Engineering, pp. 1–8.

Loughlin, C.D.O., 2018. Interpretation of free fall penetrometer tests in sands: An approach to determining the equivalent static resistance Free fall penetrometer tests in sand: Determining the equivalent static resistance.

Mabsout, M., Tassoulas, J., 1994. A Finite element model for the simulation of pile driving. Int. J. Numer. Meth. Eng. 37, 257–278.

Mitchell, J.K., Soga, K., 1976. Fundamentals of soil behavior. Number 2, 111–130.

Moavenian, M.H., Nazem, M., Carter, J.P., Randolph, M.F., 2016. Numerical analysis of penetrometers free-falling into soil with shear strength increasing linearly with depth. Comput. Geotech. 72, 57–66.

Nazem, M., Carter, J., Airey, D., Chow, S., 2012. Dynamic analysis of a smooth penetrometer free-falling into uniform clay. G´eotechnique 62, 893–905.

Omidvar, M., Iskander, M., Bless, S., 2012. Stress-strain behavior of sand at high strain rates. Int. J. Impact Eng. 49, 192–213.

Phuong, N.T.V., van Tol, A.F., Elkadi, A.S.K., Rohe, A., 2016. Numerical investigation of pile installation effects in sand using material point method. Comput. Geotech. 73, 58–71.

Rots, J., Nauta, P., Kuster, G., Blaauwendraad, J., 1985. Smeared crack approach and fracture localization in concrete. HERON, 3–48.

Sabetamal, H., Carter, J.P., Nazem, M., Sloan, S.W., 2016. Coupled analysis of dynamically penetrating anchors. Comput. Geotech. 77, 26–44.

Sabetamal, H., Carter, J.P., Sloan, S.W., 2018. Pore pressure response to dynamically installed penetrometers. Int. J. Geomech. 18, 1–16.

Sabetamal, H., Nazem, M., Carter, J.P., 2013. Numerical Analysis of Torpedo Anchors, 621–632.

Salgado, R., 2008. The engineering of foundations, vol. 888. McGraw-Hill, New York.

Seed, H.B., Lungren, R., 1954. Investigation of the effect of transient loading on the strength and deformation characteristics of saturated sands. Proc. Am. Soc. Testing Mater. 54, 1288–1306.

Smith, I.M., Chow, Y.K., 1982. Three-Dimensional Analysis of Pile Drivability. Proceedings of the 2nd International Conference on Numerical Methods in Offshore Piling , 1–20.

Soga, K., Alonso, E., Yerro, A., Kumar, K., Bandara, 2015. Trends in large-deformation analysis of landslide mass movements with particular emphasis on the material point method. Geotechnique 66, 248–273. doi: 10. 1680/jgeot.15.LM.005.

Stark, N., Hay, A.E., Trowse, G., 2014. Cost-effective geotechnical and sedimentological early site assessment for ocean renewable energies. OCEANS 2014 000.

Stark, N., Wilkens, R., Ernstsen, V.B., Lambers-Huesmann, M., Stegmann, S., Kopf, A., 2012. Geotechnical properties of sandy seafloors and the consequences for dynamic penetrometer interpretations: quartz sand versus carbonate sand. Geotech. Geol. Eng. 30, 1–14.

Stoll, R.D., Sun, Y.F., Bitte, I., 2007. Seafloor properties from penetrometer tests. IEEE J. Oceanic Eng. 32, 57–63. https://doi.org/10.1109/JOE. 2007.890943.

Suescun-Florez, E., Iskander, M., Bless, S., 2015. A model to predict strain rate dependency of dry silica sand in triaxial compression. J. Dyn. Behav. Mater. 1, 447–461.

Sulsky, D., Zhou, S., Schreyer, H.L., 1995. Application of a particle-in-cell method to solid mechanics. Comput. Phys. Commun. 87, 236–252.

Tran, Q.A., So lowski, W., 2019. Generalized Interpolation Material Point Method modelling of large deformation problems including strain-rate effects Application to penetration and progressive failure problems. Comput. Geotech. 106, 249–265.

Tran, Q.A., Solowski, W., Karstunen, M., Korkiala-Tanttu, L., 2017. Modelling of Fall-cone Tests with Strain-rate Effects. Procedia Eng. 175, 293–301.

Vesic, A.S., 1973. Analysis of ultimate loads of shallow foundations. J. Soil Mech. Foundations Div 99.

Wallstedt, P., Guilkey, J., 2008. An evaluation of explicit time integration schemes for use with the generalized interpolation material point methodAn evaluation of explicit time integration schemes for use with the generalized interpolation material point method. J. Comput. Phys. 227, 9628–9642.

Wang, D., Bienen, B., Nazem, M., Tian, Y., Zheng, J., Pucker, T., Randolph, M.F., 2015. Large deformation finite element analyses in geotechnical engineering. Comput. Geotech. 65, 104–114.

Xu, T.H., Zhang, L.M., 2015. Numerical implementation of a bounding surface plasticity model for sand under high strain-rate loadings in LSDYNA. Comput. Geotech. 66, 203–218.

Yamamuro, J.A., Abrantes, A.E., Lade, P.V., 2011. Effect of strain rate on the stress-strain behavior of sand. J. Geotech. Geoenviron. Eng. 137, 1169–1178.

Yerro, A., 2015. MPM modelling of landslides in brittle and unsaturated soils. Ph.D. thesis. Universitat Politecnica de Catalunya.

Yerro, A., Alonso, E., Pinyol, N., 2015. The material point method for unsaturated soils. G´eotechnique 65, 201–217.

Yerro, A., Alonso, E.E., Pinyol, N.M., 2016. Run-out of landslides in brittle soils. Comput. Geotech. 80, 427–439.

Zabala, F., Alonso, E., 2011. Progressive failure of Aznalco´llar dam using the material point method. G´eotechnique 61, 795–808.

Zambrano-Cruzatty, L., Yerro, A., 2019. Numerical Simulation of a Free Fall Penetrometer Deployment Using the Material Point Method. In: 2nd International Conference on the Material Point Method for Modelling SoilWater-Structure Interaction, pp. 250–256.

Zhang, H.W., Wang, K.P., Chen, Z., 2009. Material point method for dynamic analysis of saturated porous media under external contact/impact of solid bodies. Comput. Methods Appl. Mech. Eng. 198, 1456–1472.

Zhang, X., Sze, K.Y., Ma, S., 2006. An explicit material point finite element method for hyper-velocity impact. Int. J. Numer. Meth. Eng. 66, 689–706.

Zhou, S., Stormont, J., Chen, Z., 1999. Simulation of geomembrane response to settlement in landfills by using the material point method. Int. J. Numer. Anal. Meth. Geomech. 23, 1977–1994.